Analysis of carbon-binder domain morphology and correlation to effective ion transport properties

Mrudula Prasad[a,b], Benedikt Prifling[c], Matthias Neumann[d], Simon Hein[a,b], Rares Scurtu[e], Alice Hoffmann[e], André Hilger[f], Markus Osenberg[f], Ingo Manke[f], Margret Wohlfahrt-Mehrens[e], Volker Schmidt[c], Arnulf Latz[a,b,g], Timo Danner[a,b,*]

[a]*German Aerospace Center (DLR), Institute of Engineering Thermodynamics,Pfaffenwaldring 38-40,70569 Stuttgart, Germany*
[b]*Helmholtz-Institut Ulm für Elektrochemische Energiespeicherung (HIU), Helmholtzstraße 11, 89081 Ulm, Germany*
[c]*Ulm University (UUlm), Institute of Stochastics, Helmholtzstraße 18, 89081 Ulm, Germany*
[d]*Graz University of Technology, Institute of Statistics, Kopernikusgasse 24/III, 8010 Graz, Austria*
[e]*ZSW-Zentrum für Sonnenenergie- und Wasserstoff-Forschung Baden-Württemberg, Helmholtzstraße 8,89081 Ulm, Germany*
[f]*Helmholtz-Zentrum Berlin für Materialien und Energie, Hahn-Meitner-Platz 1, 14109 Berlin, Germany*
[g]*Ulm University (UUlm), Institute of Electrochemistry, Albert-Einstein-Allee 47, 89081 Ulm, Germany*

Abstract

The conductive additive and binder domain is an essential component of lithium-ion battery electrodes. It enhances the electrical connectivity and mechanical stability within the solid electrode matrix. The CBD aggregate exhibits inner porosity that significantly impacts ion transport within the electrode. Thus, the spatial distribution of CBD and its morphology play a critical role for ion transport pathways within the electrode. In order to quantify the extent of this influence, we employ high-resolution focused ion beam/scanning electron microscopy (FIB-SEM) imaging and isolate regions with just solid CBD and pore. This enables us to quantitatively correlate the CBD morphology with physical transport parameters and present a function that describes the relationship between CBD porosity and its ionic conductivity. Through our work, we provide insights into the CBD microstructure for use in future continuum-scale models.

1. Introduction

A lithium-ion (Li-ion) battery cathode typically consists of four phases: the cathode active material (CAM), conductive additive and binder (CBD) and electrolyte. The conductive additive assists in the formation of short- and long-range electronic networks as CAMs tend to have poor electronic conductivity. The binder assists in retaining the structural integrity of the solid materials within themselves and to the current collector (CC). The electrolyte wets the pore space and provides pathways for ion transport. Typically, conductive additives and binder form a composite conductive additive and binder domain (CBD) within the cathode microstructure. The influence of a macroscopic distribution of the CBD within the electrode has been dealt with in previous literature [1, 2, 3, 4, 5], where the effect of varying CBD spatial distribution on cathode performance is analysed.

In this work, we focus on the microstructure properties of the CBD. More specifically, we investigate the relation between structural properties and the ionic conductivity within the electrolyte-filled pore space of the CBD, relative to the bulk electrolyte conductivity [6, 7, 8, 9, 10, 11, 12, 13]. When possible, the properties will be compared in terms of an ionic conductivity, unless tortuosity factors are instead provided in the literature

*Corresponding author:
Email address: timo.danner@dlr.de (Timo Danner)
URL: http://www.dlr.de/tt/en/ (Timo Danner)

and the inner CBD porosity values are not available for conversion to ionic conductivity, as per Equation 1. The focus of this work is to derive correlations between structure, that is local variations within the CBD, and effective transport properties. Quantification of CBD morphology and corresponding transport properties is challenging and attempts based on virtually created electrodes [8, 12, 14, 15, 16] combined with inverse analysis [6], mercury intrusion porosimetry (MIP) [13, 17], or high-resolution image data [7, 10, 18], are presented in the literature. Usseglio-Viretta et al. generated synthetic electrodes within a porosity range of 33% and 52% with varying CBD volume fractions and pore morphological parameter. They determined an effective ion tortuosity for the CBD phase, τ, between 1.42 and 1.81 assuming the CBD homogeneously fills macropores [14]. Ge et al. go a step further and inform their virtual CBD microstructure with the effective electrode tortuosity values measured by [14] using electrochemical impedance on symmetric cells [12]. An effective electrode ion tortuosity value, τ, between 1.6 and 2.4 for CBD porosity between 30% and 60% was proposed adhering to the following function: $\tau = 0.72\epsilon^{-0.97}$, where ϵ is the total volume fraction of pores (mesopores in the CBD and the macropores). Srivastava et al. [19] cite an effective electrode ion tortuosity between 2.0 and 4.5 for an electrode porosity between 30% and 50%, and follow that the CBD has an internal porosity of 50% as per [18]. In order to isolate the effect of the CBD, Vierrath et al. utilized image reconstruction techniques suggesting a relative ion transport conductivity within the CBD phase between 30 to 37% for an LiCoO$_2$ cathode [7]. They compare their results to Stephenson et al.. Stephenson et al. calculated, from restricted-diffusion experiments [20], for two films with a binder-to-carbon ratio of 63:37 and 46:54, a domain intrinsic electrolyte conductivity between 3 to 5%, respectively. Vierrath et al. correspondingly attribute their higher conductivity values to absence of binder swelling and correct the CBD internal porosity to 17% to achieve the same average CBD tortuosity as the experiments by [10]. Further work to isolate the effects of the CBD has been done by Zielke et al. [17]. They analyse artifically generated CBD nanoscale structures and suggest that the CBD ionic conductivity lies between 5% and 25% of the bulk electrolyte conductivity within electrode porosities of 32% to 40%. Pinilla 2025 et.

al. attempt to characterise the inner porosity of the CBD phase by comparing simulation with experimental data [21]. They suggest a homogeneous CBD internal porosity between 50 to 60%. They generate stochastic structures with varying internal CBD porosities, and examine their influence on the electrode-level tortuosity. The best match of each tortuosity to the corresponding experimentally extracted tortuosity, via symmetric cell impedance measurements under specific assumptions, hints at the possible CBD internal porosity for that manufactured electrode. Which presents the challenge of requiring experimental data for each electrode simulated. As several of these publications address reconstructing or distributing the CBD in the electrode, Prifling et al. [6] considered four different approaches to the macroscopic CBD distribution in cathode tomographic image data. They then fit the effective ion transport in the CBD phase for each approach by comparing the output of half-cell (HC) simulations with experiments. For CBD reconstructed via information from EDX data, the relative ionic conductivity was 8.9%, whereas that reconstructed by a feed-forward neural network (conditioned in the sequence: CAM-CBD-Pore) gave a lower factor at 4.5%, assuming for both cases a homogeneous internal porosity of 50% for single-layer electrodes.

Although these studies provide values to quantify the CBD internal porosity and its corresponding tortuosity, insight into the heterogeneity of its microstructure, and extraction of parameters directly from real-electrode data is missing; the latter automatically considering the CBD internal porous pathways. In this publication, we want to focus on the local CBD properties. More specifically, we determine structural properties of CBD volume elements (i.e. its internal porosity range, pore size distribution) and correlate them to a relevant transport parameter. Relative values are provided, as local measurements of conductivity to determine bulk values are very challenging. Atomic Force Microscopy (AFM) is reported in literature [22, 23, 24, 25] to determine electric conductivity of materials, however it has, to our knowledge, not been applied to conductive additive networks in Lithium-ion batteries. Furthermore, for the pore phase, the absolute conductivity will depend on the electrolyte system. Based on high-resolution (10 nm) FIB-SEM tomography data of a dry electrode sample, we extract the CBD pore network. On

this data, we perform an in-depth analysis of structural and transport properties providing detailed insights on the effect of local CBD parameters. Understanding the effect of the internal microstructure of CBD is relevant for the optimization of production processes and and for improving the predictability of continuum models.

2. Methods

A flowchart of the methods used in this work is shown in Figure 1. The subsequent sections are subdivided as indicated in this flowchart.

Electrode material composition

The exact manufacturing information to the electrode studied here is provided in [6], denoted under Suspension D in their paper. A short summary of the material fractions is provided here in Table 1.

3D FIB-SEM imaging and reconstruction

The analysis in this work is done on the FIB-SEM data provided by Prifling *et al.* [6]. The FIB-SEM tomography has been conducted at the Helmholtz-Zentrum Berlin (HZB) using the ZEISS Crossbeam 340. The pixel size was set to 10 nm, which also corresponds to the thickness of the slices that have been cut by the FIB. The active material was segmented using a global Otsu threshold, whereas a U-Net was used to differentiate between pore and solid phases. Detailed information regarding the segmentation process is provided in [6].

Extraction and processing of CBD domains

From the FIB-SEM data, 151 cubic cutouts of length 1.28 μm (corresponding to 128 voxels) consisting of only CBD and pore space, devoid of any CAM, were extracted (as shown in Figure 1 (a)). Such a cubic cutout is equivalent to one voxel in the synchrotron tomography image of the same electrode (studied in [6]). Hence, this CBD cutout size was chosen so that the data analysed in this study could be applied to the synchrotron image in future work. Throughout this paper, these volumes with resolved solid CBD and pore space are referred to as CBD cutouts. For details on the extraction and pre-processing of the image data, refer to the Supporting Information (SI) Section 1.

Manufactured electrode data	
Electrode density (g/cm^3)	3.06
Mass loading (mg/cm^2)	49.1
Material	Fraction (vol.-%)
NMC622 (BASF)	59.5
Carbon black (SuperP, Imerys)	3.31
Graphite (SFG6L, Imerys)	1.35
PVDF (Solvay Solexis)	6.88
Porosity	28.9
FIB-SEM data	
Resolution (nm)	10
Direction (see Figure 1 (a))	$x \times y \times z$
Dimensions (μm)	$27.20 \times 15.31 \times 14.36$
Material	Fraction (vol.-%)
CAM	57.5
CBD	15.8
Porosity	26.8

Table 1: Information regarding the electrode, which underlies the present study, and the corresponding FIB-SEM data. NMC622 stands for LiNi$_{0.6}$Co$_{0.2}$Mn$_{0.2}$O$_2$ CAM, and PVDF for polyvinylidene fluoride. Given in brackets are the manufacturers.

Selection of representative CBD domains

In order to differentiate between macropores and the mesoporosity of the CBD, we extend the original CBD cutouts with its neighbouring voxels from the FIB-SEM data. This extended region of volume 800^3 voxels envelopes the original 128^3 voxels geometry, allowing for a better analysis of the connected pore space. In a second step we use a watershed algorithm [28, 27] to identify individual pores within the enveloping domain and determine corresponding pore volumes, centers and connectivities. Depending on the position of pore centers and pore volumes with respect to the original 128^3 voxels CBD cutout, these metrics serve as a filter for macroporous regions. We utilised this method to filter the domains in-contrast to simple image-closing techniques, as it is more physically-informed. For the chosen metrics and its corresponding impact on the selection of representative CBD cutouts, we refer the interested reader to the SI Sections 4 and 5.
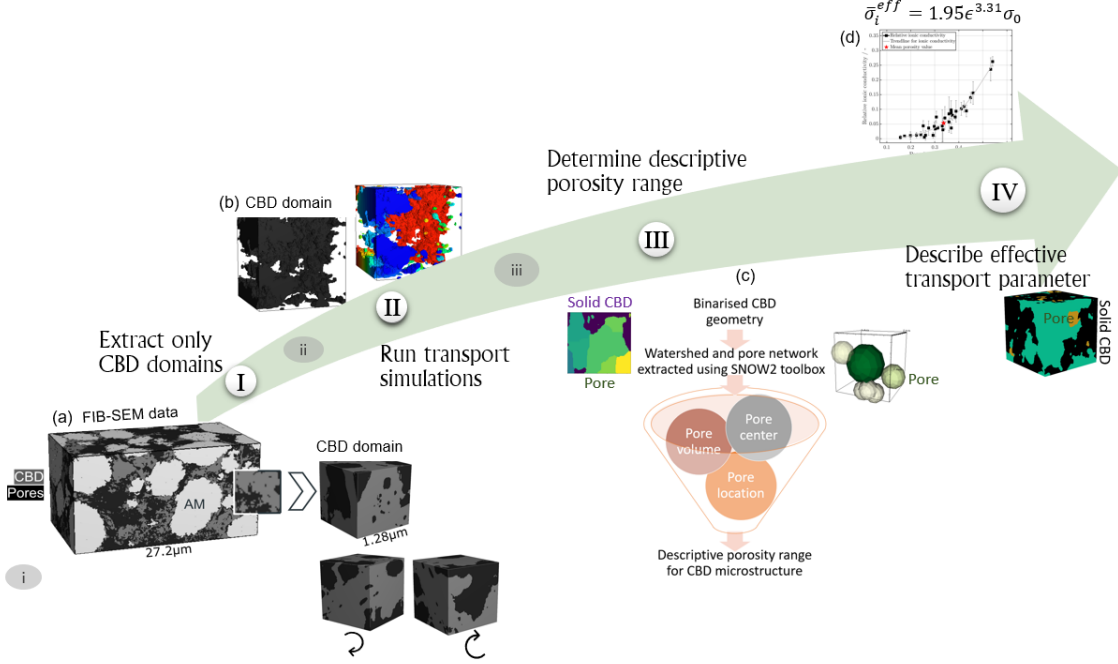
Figure 1: Flowchart of sequential numerical methods employed in the current study to determine the representative CBD microstructure. Lower case Roman numbers indicate intermediate steps, and the upper-case numerals indicate the main steps. (i) is the segmentation of the FIB-SEM raw data using U-Net [6] (see Section 3D FIB-SEM imaging and reconstruction). In black is the porous space, in gray is the CBD phase, and the AM is given in white. (I) shows the extraction of the CBD volumes from the FIB-SEM data using MATLAB. Each cutout is rotated across an axis to analyse anisotropy (see Section Extraction and processing of CBD domains). In (ii) image processing steps are applied to remove artifacts prior to running simulations. (II) exemplifies potential distribution across a CBD cutout when determining the relative ionic conductivity via the BEST [26] software (see Section Transport simulations on the CBD domains). Extracted CBD cutouts from (I) are extended in (iii) to include neighboring voxels to better assign pore length-scale (see Supporting Information Section 3). (III) depicts the 2D slice of a CBD cutout, its segmentation and subsequent pore network extraction using the SNOW2 [27] algorithm in PoreSpy (see Section Selection of representative CBD domains). In green colour shade is the pore space, and in blue is the solid CBD. Finally (d) shows the CBD representative porosity range (see Section Correlation of effective transport parameters).

Transport simulations on the CBD domains

To determine the relative ion conductivities of the CBD cutouts, the steady-state Poisson equation is solved with a constant current density boundary condition applied on the two opposite planes normal to the direction of interest [9]. A zero-flux boundary condition is applied to the faces orthogonal to the investigated direction. Focus of this work is on the relative ionic conductivity of the CBD, $\sigma_{\mathbf{x},i}^{eff}/\sigma_0$. The electronic conductivities of CBD cutouts are provided in the SI Section 7. The ion tortuosity, $\tau_{\mathbf{x},i}$ for each CBD cutout i, and the three spatial coordinates $\mathbf{x}$ was then calculated according to Equation 1, where ϵ_i is the porosity in each unique volume (CBD cutout), i, and

σ_0 is the ion conductivity in the bulk electrolyte. Further details on the simulation setup are provided in the SI Section 6.

$$\sigma_{\mathbf{x},i}^{eff} = \frac{\epsilon_i}{\tau_{\mathbf{x},i}}\sigma_0 \tag{1}$$

Correlation of effective transport parameters

In literature, the Bruggeman correlation is often used to describe the dependence of effective transport parameters on porosity or volume fraction for electrodes with homogeneously distributed particles. It is also known to

4

overestimate effective conductivities [17, 29, 30]. However, the ansatz still holds and we use this to fit the trend of relative conductivity as a function of porosity given by this power law function: (2).

$$\frac{\sigma_{\mathbf{x},i}^{eff}}{\sigma_0} = \frac{\epsilon_i}{\tau_{\mathbf{x},i}} = \gamma \epsilon_i^{\alpha} . \tag{2}$$

Where the Bruggeman correlation is derived for a dense packing of spherical particles, (leading to $\gamma=1$, $\alpha=1.5$), we attempt to derive the exponents without making inherent assumptions on the material structure, packing and distribution.

3. Results and discussion

Here, we will present the porosity distribution of CBD cutouts, results of the ion transport simulations, and finally, a function to describe the relative ion transport within the CBD phase as a function of its porosity.

Relative ion conductivity of all CBD domains

The result of the transport simulations is shown in Figure 2 (a). As expected, it follows the trend given by Equation 2. The ionic conductivity as an average of three data points for simulations run across each spatial dimension is shown in the black square markers, along with the standard deviation indicating anisotropic transport.

There is a wide distribution of the porosities, ensuring a large data set for further analyses from different regions of the electrode (refer to the SI Section 1). Figure 2 (a) shows an accumulation of data points between 14% to 60% porosity, and a second cluster of CBD cutouts at porosities higher than 90%. The mean porosity when considering all CBD cutouts lies at 64.11% and the corresponding tortuosity for ion transport in the CBD phase is 1.85 (or an relative ionic conductivity of 0.35). This value is close to the Bruggeman-corrected tortuosity of 1.41, which is known to overestimate the electrode performance [17, 29, 30].

Relative ion conductivity of selected CBD domains

Figure 3 shows the conductivities from Figure 2(a), but restricted to just the selected domains. Each solid black symbol represents one CBD cutout. Applying the metrics described in SI Sections 4 and 5 removes all CBD cutouts with porosities larger than 56%. The arithmetic mean porosity and ion tortuosity of the selected domains lie at 33.68% and 6.41, respectively. The ion tortuosity is almost 3.5 times higher than the average calculated when considering all the domains (1.85), and the Bruggeman-corrected value (1.41) at 50% internal porosity. The method used here to define the CBD ion transport parameter accounts for the anisotropy in its morphology and does not assume a uniform volume-average tortuosity value.

The weighted power law fit in Equation 3 is suggested as a description of the ionic conductivity across the CBD porosity range from 14 % to 56% as shown in Figure 3. Above 56%, the relative ionic conductivity continues to increase with porosity, however it follows more of a linear trend. At these porosities, the extracted CBD volumes show an increasing number of low tortuosity pathways. Thus, the effective transport starts to scale with the projected blocked area resulting in a linear dependence. This is reflected in the outcome of our filtering steps, where the CBD volumes with high porosities are neglected.

$$\bar{\sigma}_i^{eff} = 1.95 \ \epsilon^{3.31} \ \sigma_0 \tag{3}$$

Other physical properties

Further information to the pore size distribution (PSD) within these selected domains can be extracted, as shown in Figure 2 (b). It illustrates the PSD determined by MIP measurements on the electrode sample (in gray) compared with simulations on the complete FIB-SEM data (in blue) and additionally, just on the selected CBD cutouts (in orange). Measurement data show a bimodal distribution with a clear peak at 1 μm which, according to [13, 31, 32], can be assigned to the intra-CAM void space. The exact region representing CBD inner PSD is challenging to define. Bockholt et al. and Mayer at al. show that altering the manufacturing process influences the homogeneity and structure of the CBD phase [13, 33]. However,
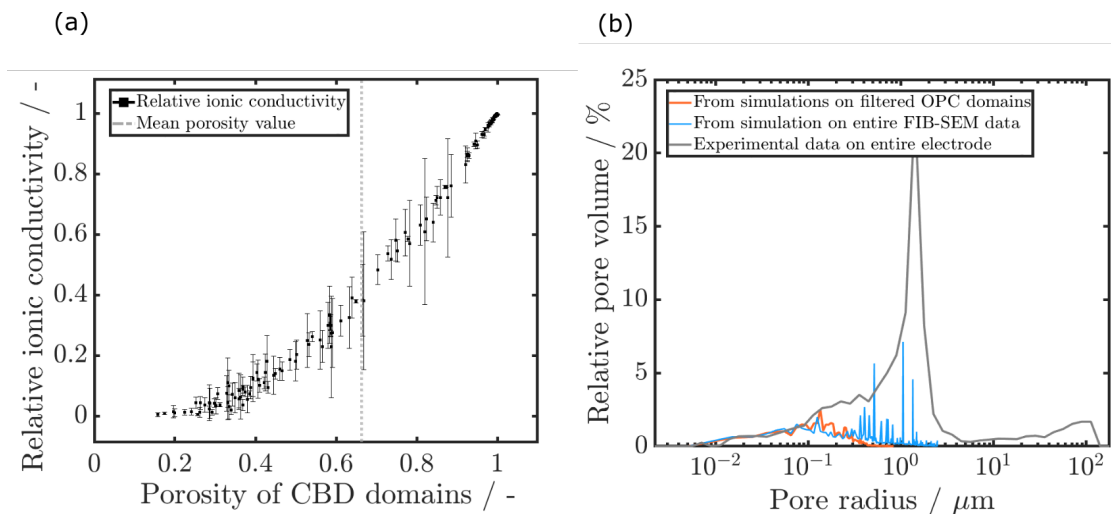
5

(a)   (b)

Figure 2: (a) The relative ionic conductivities in all the CBD cutouts as a function of their porosities. The vertical line in gray is the arithmetic mean porosity value. (b) Results of the mercury porosimetry simulations using GeoDict conducted on the complete FIB-SEM volume (blue) and the sum over all selected CBD cutouts (orange), compared to the experimental data on the entire electrode (gray). The GeoDict model used the same material wetting angle (140 degrees) and surface tension (0.48 Nm) properties as used in the experiments. By running the porosimetry simulations on just the selected CBD cutouts, we are able to more confidently assign the pore size distribution range corresponding to porous CBD. This comparison shows a good accordance regarding the left-tails of these distributions, which quantify the pore morphology on the nano-scale, i.e. the length-scale of interest. The pore volumes of selected data (in orange) were normalised to the FIB-SEM data volume.

since a mixing time for more than 2 mins was used for the slurry in our study [33], the peaks around 0.1 µm can be attributed to the porous space within the CBD cutout [13, 34]. In the simulations on the whole FIB-SEM domain, we similarly observe a maximum in the pore size distribution at 0.1 µm and several peaks at larger pore sizes. Note, that the small volume of the FIB-SEM data allows for only limited statistics in this region. Still, the PSD determined on the final filtered selection of CBD cutouts (orange line) agrees well with the data on the whole FIB-SEM image. This indicates a suitable selection of CBD inner-pore selection criteria in our study, and confirms interpretation of the MIP data. Moreoever, MIP data can be used to determine a volume-averaged inner carbon black porosity in the electrode at the absence of high-resolution FIB-SEM images, allowing the Equation 3 to be applied.

Discussion and comparison to literature

Figure 4 compares the relative ion conductivity values determined by the various publications to this study. We take references from the literature that have specifically

endeavoured to extract the CBD internal porosity and its relative ion transport parameter.

The range of values suggested by Vierrath et al., via image processing, lie close to the highest porosity determined from this study [7]. Eventhough they extracted 261 FIB-SEM images, the total reconstructed volume was only 0.75% of the FIB-SEM domain studied here. Hence, it is possible, that the FIB cut in [7] dominantly captured higher porosity CBD cutouts. As for the binder-carbon electrode films measured by Stephenson et al., they maintained a CBD porosity of 63% in both films [10]. This was, however, determined via image analysis on a much more porous electrode (50%) than the one studied here (28%). The absence of restricting AM could have allowed the binder to swell upon electrolyte addition, occupying available void volume, thus decreasing the conductivities measured on these films. Finally, comparing the results to that estimated and fit by Prifling et al., the relative conductivity for the EDX-informed reconstruction (8.90%) is closer to the mean from the current study (5.32%) at an internal porosity of 50%,
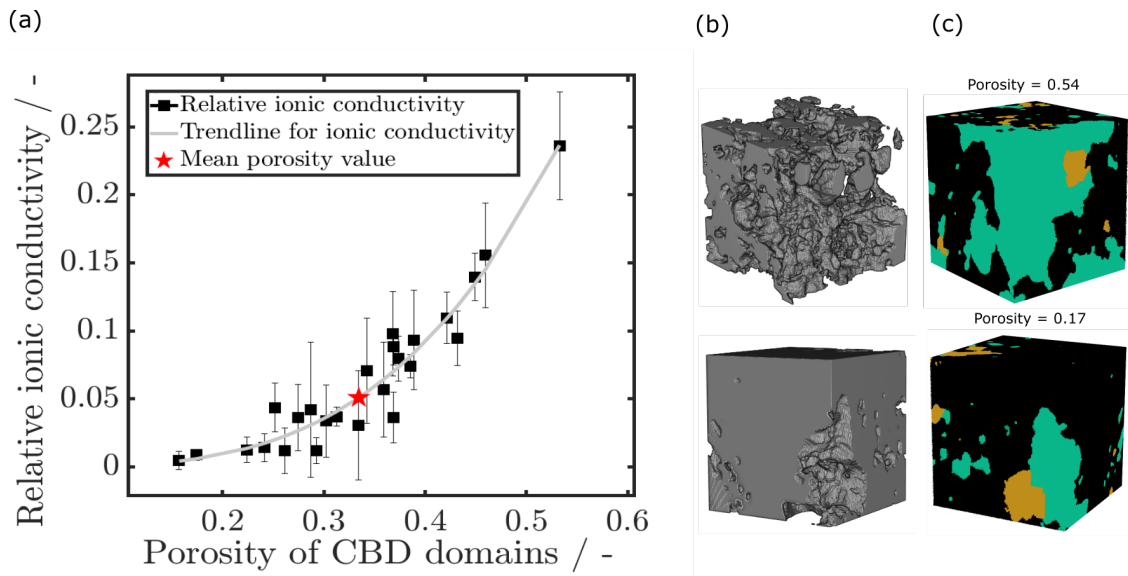
Figure 3: (a) The representative relative ionic conductivity vs porosity of the CBD cutouts once the filters detailed in Section 2 have been imposed. The trendline in gray is a weighted power law fit of the form shown in Equation 2: σ_{rel}=1.95×$\epsilon^{3.31}$. The mean porosity is shown by the red star at 33.68% and the corresponding ion tortuosity at 6.32. (b) The microstructures of the CBD for comparison at 17% and 54.10% porosity values. The invisible region is the pore space, whereas shown in gray is the solid CBD. (c) The corresponding segregated pore space of the domains shown in (b). In black is the solid space, in orange the retained pore space after conducting the metrics, and in green is the excluded pore space that is not considered as belonging to the CBD microstructure.

compared to the CBD reconstructed via neural networks. However, the ϵ/τ value of the latter (0.045) agrees well with the mean ϵ/mean τ value from this study (0.053). As seen in Equation 1, the ϵ/τ is the correction used in the theoretical models to correct for effective transport.

The advantage of our work, is that we present a distributed property for the CBD phase and analyse its morphology without assuming a homogeneous internal porosity. Comparison of the MIP simulation data on just the CBD cutouts, to experimental data on the entire electrode shows a good accordance regarding the left-tails of these distributions (see Figure 2). This further indicates that the image segmentation and subvolume size reliably reconstructs the pore space from the FIB-SEM data, and the determination criteria for inner pores within the CBD is appropriately chosen. We further conduct thorough analyses to distinguish mesopores from macropores on real electrodes, decoupled from fitting to electrochemical data. The metrics applied (see SI Section 5) were based on physical reasoning and the final PSDs match well with the experiments (see Figure 2 (b)), validating the methods used. Since a wide range of CBD cutout porosities from various spatial locations in the FIB-SEM data were considered (see SI Section 1), the suggested function covers the relevant range of porosities as reported in literature. Naturally, there are uncertainties involved in the process. The FIB-SEM data covers only a fraction of the real electrode, and was imaged closer to the separator. The analyses were conducted on dry electrode data, without the influence of electrolyte. Still, this study is a step forward in understanding the real microstructure and effective properties of the CBD phase.

The focus of this work is first on presenting the methods for the resulting correlation for CBD morphology, which has not yet been employed in the literature. Combining imaging, and electrode scale electrochemical characterization (impedance spectroscopy on symmetric cells and rate tests) with simulation tools in data-driven approaches might be a pathway to indirectly characterize CBD properties and is something we are working on. This can then be used as a validation of the derived correlation. Linking the CBD properties to the production process is then the ultimate challenge. We plan to use our simulation tool to more accurately predict improved CBD distribu-
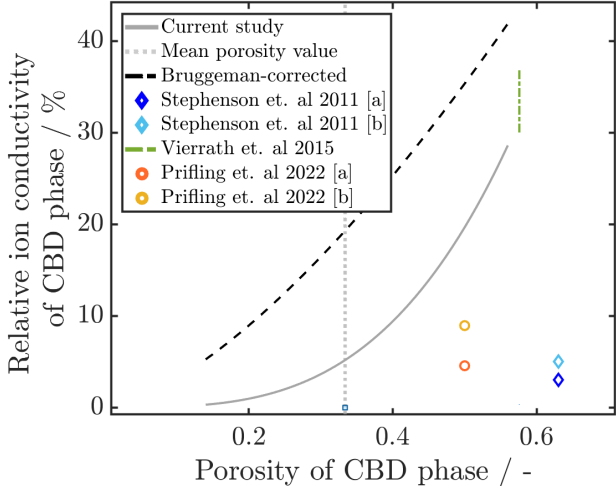

Figure 4: Shows the relative ion conductivity determined from other studies, in color, compared to the one suggested here, in gray. As the dotted gray line is the mean porosity value from the current study (Figure 3). Additionally, the function for a Bruggeman-corrected conductivity value assuming the CBD can be described as a homogeneously distributed, spherical particle, is plotted in black. Stephenson et al. measured conductivities at two binder-to-carbon ratios in pure CBD films [10]. [a] is at 63:37 binder-to-carbon ration, where [b] is at 46:54 binder-to-carbon ratio. The post image-processing value determined by Vierrath et al. before fitting to the measurements by [10] is plotted [7]. Prifling at. al suggest varying conductivities based on CBD reconstruction method. [a] is the conductivity for CBD distributed via a neural network, where the CAM is thresholded first, then the CBD and finally, the pore space. [b] is the conductivity for an EDX-informed reconstruction [6].

tions. However, connecting them to processing conditions will require more characterization work using a scheme as discussed above, or combining our work with actual production simulations predicting CBD morphology [35].

Additional geometric properties such as the pore size distribution from the segmented data, the morphology (possible shape) of the pore space, active surface area, and the electronic conductivites are provided in the SI Section 7.

4. Conclusion

In this paper, we investigate the inner carbon black porosity which is a critical parameter for ion transport

within the electrode matrix. By close inspection of high-resolution FIB-SEM data, we identify CBD cutouts with a porosity range between 14% to 56%, and an intrinsic conducting pore diameter distribution between 60 to 400 nm. Based on the image data we performed conductivity calculations providing a correlation between CBD porosity and relative ionic conductivity which can be described by a power law ansatz according to $\bar{\sigma}_i^{eff} = 1.95 \ \epsilon^{3.31} \ \sigma_0$. Relative values are provided as local measurements of conductivity to determine bulk values are very challenging. Additional parameters such as the pore size distribution, specific surface area and relative electronic conductivity are provided in the Supporting Information. These quantities are essential input for predictive continuum simulations on the electrode and cell level. Although the pore size distribution is smaller than the synchrotron image resolution, the data suggests that a porosity distribution within the CBD phase exists, which can be reconstructed based on the synchrotron gray-scale values. This shows variations in the density and thus, the porosity of the CBD phase. The effect of this porosity distribution of the CBD within the electrode is planned to be investigated in a subsequent publication which is currently under preparation. In our previous publication, we have considered the influence of a macroscopic distribution of the CBD on the electrode performance; where an accumulation of binder at the separator inhibited ion penetration at higher C-rates, and a higher fraction of conductive additive at the current collector increased current flux by lowering contact resistance. As mentioned previously, the focus of this paper is to extract structural properties and relate it to a physical transport parameter. In future work, we will be looking at a distributed CBD porosity across the electrode to examine its effect on performance. The effect of the porosity distribution of the CBD within the electrode is planned to be investigated in a subsequent publication which is currently under preparation. These additional simulations will beTherefore, the current work provides essential information enabling a step forward in understanding the influence of the distribution of the CBD properties across the electrode and aid in future fabrication of battery electrodes.

References

[1] R. Morasch, J. Landesfeind, B. Suthar, H. A. Gasteiger, Detection of binder gradients using impedance spectroscopy and their influence on the tortuosity of Li-ion battery graphite electrodes, Journal of the Electrochemical Society 165 (14) (2018) A3459–A3467.

[2] A. Shodiev, E. N. Primo, M. Chouchane, T. Lombardo, A. C. Ngandjong, A. Rucci, A. A. Franco, 4D-resolved physical model for electrochemical impedance spectroscopy of $Li(Ni_{1-x-y}Mn_xCo_y)O_2$ - based cathodes in symmetric cells: Consequences in tortuosity calculations, Journal of Power Sources 454 (2020) 227871.

[3] J. Landesfeind, A. Eldiven, H. A. Gasteiger, Influence of the binder on lithium ion battery electrode tortuosity and performance, Journal of the Electrochemical Society 165 (5) (2018) A1122–A1128.

[4] B. Prifling, M. Röding, P. Townsend, M. Neumann, V. Schmidt, Large-scale statistical learning for mass transport prediction in porous materials using 90,000 artificially generated microstructures, Frontiers in Materials 8 (12 2021).

[5] M. Prasad, S. Hein, T. Danner, B. Prifling, R. Scurtu, A. Hoffmann, A. Hilger, M. Osenberg, I. Manke, M. Wohlfahrt-Mehrens, V. Schmidt, A. Latz, Influence of conductive additives and binder on the impedance of lithium-ion battery electrodes: Effect

of an inhomogeneous distribution, Journal of The Electrochemical Society 171 (2024) 100518.

[6] B. Prifling, M. Neumann, S. Hein, T. Danner, E. Heider, A. Hoffmann, P. Rieder, A. Hilger, M. Osenberg, I. Manke, M. Wohlfahrt-Mehrens, A. Latz, V. Schmidt, Quantitative comparison of different approaches for reconstructing the carbon-binder domain from tomographic image data of cathodes in lithium-ion batteries and its influence on electrochemical properties, Energy Technology 11 (5) (2023) 2200784.

[7] S. Vierrath, L. Zielke, R. Moroni, A. Mondon, D. R. Wheeler, R. Zengerle, S. Thiele, Morphology of nanoporous carbon-binder domains in Li-ion batteries - A FIB-SEM study, Electrochemistry Communications 60 (2015) 176–179.

[8] B. L. Trembacki, A. N. Mistry, D. R. Noble, M. E. Ferraro, P. P. Mukherjee, S. A. Roberts, Mesoscale analysis of conductive binder domain morphology in lithium-ion battery electrodes, Journal of The Electrochemical Society 165 (2018) E725–E736.

[9] T. Knorr, S. Hein, B. Prifling, M. Neumann, T. Danner, V. Schmidt, A. Latz, Simulation-based and data-driven techniques for quantifying the influence of the carbon binder domain on electrochemical properties of Li-ion batteries, Energies 15 (2022) 7821.

[10] D. E. Stephenson, B. C. Walker, C. B. Skelton, E. P. Gorzkowski, D. J. Rowenhorst, D. R. Wheeler, Modeling 3D microstructure and ion transport in porous Li-ion battery electrodes, Journal of The Electrochemical Society 158 (2011) A781.

[11] W. Wu, F. Jiang, Simulated annealing reconstruction and characterization of the three-dimensional microstructure of a $LiCoO_2$ lithium-ion battery cathode, Materials Characterization 80 (2013) 62–68.

[12] R. Ge, A. M. Boyce, Y. Sun, P. R. Shearing, P. S. Grant, D. J. Cumming, R. M. Smith, Numerical design of microporous carbon binder domains phase in composite cathodes for lithium-ion batteries, ACS Applied Materials & Interfaces 15 (23) (2023) 27809–27820.

[13] J. K. Mayer, H. Bockholt, A. Kwade, Inner carbon black porosity as characteristic parameter for the microstructure of lithium-ion electrodes and its effect on physical and electrochemical properties, Journal of Power Sources 529 (231259) (2022).

[14] F. L. E. Usseglio-Viretta, A. Colclasure, A. N. Mistry, K. P. Y. Claver, F. Pouraghajan, D. P. Finegan, T. M. M. Heenan, D. Abraham, P. P. Mukherjee, D. Wheeler, P. Shearing, S. J. Cooper, K. Smith, Resolving the discrepancy in tortuosity factor estimation for Li-ion battery electrodes through micro-macro modeling and experiment, Journal of The Electrochemical Society 165 (2018) A3403–A3426.

[15] A. N. Mistry, K. Smith, P. P. Mukherjee, Secondary-phase stochastics in lithium-ion battery electrodes, ACS Applied Materials & Interfaces 10 (2018) 6317–6326.

[16] P. Gräfensteiner, M. Osenberg, A. Hilger, N. Bohn, J. R. Binder, I. Manke, V. Schmidt, M. Neumann, Data-driven stochastic 3D modeling of the nanoporous binder-conductive additive phase in battery cathodes (2024). `arXiv:2409.11080`. URL https://arxiv.org/abs/2409.11080

[17] L. Zielke, T. Hutzenlaub, D. R. Wheeler, C. W. Chao, I. Manke, A. Hilger, N. Paust, R. Zengerle, S. Thiele, Three-phase multiscale modeling of a $LiCoO_2$ cathode: Combining the advantages of FIB-SEM imaging and X-ray tomography, Advanced Energy Materials 5 (2015).

[18] A. M. Grillet, T. Humplik, E. K. Stirrup, S. A. Roberts, D. A. Barringer, C. M. Snyder, M. R. Janvrin, C. A. Apblett, Conductivity degradation of polyvinylidene fluoride composite binder during cycling: Measurements and simulations for lithium-ion batteries, Journal of The Electrochemical Society 163 (2016) A1859–A1871.

[19] I. Srivastava, D. S. Bolintineanu, J. B. Lechman, S. A. Roberts, Controlling binder adhesion to impact electrode mesostructures and transport, ACS Applied Materials & Interfaces 12 (31) (2020) 34919–34930.

[20] I. V. Thorat, D. E. Stephenson, N. A. Zacharias, K. Zaghib, J. N. Harb, D. R. Wheeler, Quantifying tortuosity in porous Li-ion battery materials, Journal of Power Sources 188 (2009) 592–600.

[21] S. Pinilla, F. M. Zanotto, D. Z. Dominguez, T. García, A. A. Franco, Carbon-binder-domain porosity extraction through lithium-ion battery electrode impedance data, Energy Storage Materials 74 (2025) 103818.

[22] A. Vetushka, T. Itoh, Y. Nakanishi, A. Fejfar, S. Nonomura, M. Ledinský, J. Kočka, Conductive atomic force microscopy on carbon nanowalls, Journal of Non-Crystalline Solids 358 (17) (2012) 2545–2547.

[23] J. Entwistle, R. Ge, K. Pardikar, R. Smith, D. Cumming, Carbon binder domain networks and electrical conductivity in lithium-ion battery electrodes: A critical review, Renewable and Sustainable Energy Reviews 166 (2022) 112624.

[24] W. Zhao, W. Song, L.-Z. Cheong, D. Wang, H. Li, F. Besenbacher, F. Huang, C. Shen, Beyond imaging: Applications of atomic force microscopy for the study of lithium-ion batteries, Ultramicroscopy 204 (2019) 34–48.

[25] A. Mascaro, Y. Miyahara, T. Enright, O. E. Dagdeviren, P. Grütter, Review of time-resolved non-contact electrostatic force microscopy techniques with applications to ionic transport measurements, Beilstein Journal of Nanotechnology 10 (2019) 617–633.

[26] Fraunhofer Institute for Industrial Mathematics (ITWM), BEST - Battery and Electrochemistry Simulation Tool (2020).
URL http://itwm.fraunhofer.de/best

[27] J. Gostick, Z. Khan, T. Tranter, M. Kok, M. Agnaou, M. Sadeghi, R. Jervis, Porespy: A python toolkit for quantitative analysis of porous media images, Journal of Open Source Software 4 (2019) 1296.

[28] J. T. Gostick, Versatile and efficient pore network extraction method using marker-based watershed segmentation, Physical Review E 96 (023307) (2017).

[29] R. Ge, D. J. Cumming, R. M. Smith, Discrete element method (DEM) analysis of lithium ion battery electrode structures from X-ray tomography - The effect of calendering conditions, Powder Technology 403 (2022) 117366.

[30] B. Tjaden, S. J. Cooper, D. J. Brett, D. Kramer, P. R. Shearing, On the origin and application of the Bruggeman correlation for analysing transport phenomena in electrochemical systems, Current Opinion in Chemical Engineering 12 (2016) 44–51.

[31] S. Radloff, L. S. Kremer, A. Hoffmann, M. Wohlfahrt-Mehrens, Characterization of structured ultra-thick $LiNi_{0.6}Co_{0.2}Mn_{0.2}O_2$ lithium-ion battery electrodes by mercury intrusion porosimetry, Materials Today Communications 28 (2021) 102549.

[32] A. Hoffmann, E. A. Heider, C. Dreer, C. Pfeifer, M. Wohlfahrt-Mehrens, Influence of the mixing and dispersing process on the slurry properties and the microstructure and performance of ultrathick cathodes for lithium-ion batteries, Energy Technology 11 (2200484) (2023).

[33] H. Bockholt, W. Haselrieder, A. Kwade, Intensive powder mixing for dry dispersing of carbon black and its relevance for lithium-ion battery cathodes, Powder Technology 297 (2016) 266–274.

[34] C. Meyer, H. Bockholt, W. Haselrieder, A. Kwade, Characterization of the calendering process for compaction of electrodes for lithium-ion batteries, Journal of Materials Processing Technology 249 (2017) 172–178.

[35] A. Chauhan, H. Nirschl, Numerical investigation of conductivity additive dispersion in high-power and high-energy NMC-based lithium-ion battery cathodes: Application-based guidelines, Energy Technology 11 (8) (2023) 2300281.